Stokes Flow Through a Single-Screw Extruder

M. G. Blyth
School of Mathematics, University of East Anglia, Norwich, NR4 7TJ, U.K.

C. Pozrikidis
Dept. of Mechanical and Aerospace Engineering, University of California, San Diego, La Jolla, Ca 92093

DOI 10.1002/aic.11050
Published online December 1, 2006 in Wiley InterScience (www.interscience.wiley.com).

Stokes flow through a single-screw extruder driven either by an axial pressure-gradient, or by the rotation of the screw, or by a combination of both is analyzed. The geometry of the screw is chosen to resemble that encountered in the metering section of a real-life industrial extruder. Working on the simplifying assumption of large helical pitch, a perturbation analysis is performed in non-orthogonal helical coordinates, and contributions to the velocity and pressure fields are computed up to second-order by finite element methods for unidirectional and two-dimensional Stokes flow. Velocity fields are presented for different screw geometries, the axial flow rate is computed for pressure- and rotation-driven flow, comparisons with simple models are made, and the effect of the pitch on the trajectories of passively convected particles is demonstrated. In the case of purely pressure-driven flow, the flow rate decreases, whereas in the case of rotating flow the flow rate increases as the gap between the screw and the barrel is reduced. © 2006 American Institute of Chemical Engineers *AIChE J,* 53: 69–77, 2007
Keywords: single-screw extrusion, Stokes flow, helical coordinates

Introduction

Single- and twin-screw extruders are commonly used in the manufacturing industry for a variety of purposes including the fabrication of medical tubing, the sheathing of wires and cables, and the production of medium- and low-density thermoplastic foams.[1] In a twin-screw extrusion assembly, two screws are mounted side-by-side within the same barrel. Single-screw extruders are standard equipment in the food processing industry.[2] In a conventional operation, solid material most often in the form of small polymeric pellets, is fed through a hopper onto a rotating screw that is mounted along the axis of a long barrel, as illustrated in Figure 1. The solid pellets enter the melting section, where they are heated, melted, and then passed through into the metering zone. Here, the melt is mixed prior to being ejected through the die to form the final product. In extrusion foaming, it is desirable to use a serial system in which material ejected from one extruder is fed immediately into a second extruder.[3]

The study of extrusion flows is motivated by the desire to improve efficiency and promote fluid mixing. The main advantages of the single-screw extruder are a relatively simple design, ease of manufacture, and low production cost. The screw itself is typically long and thin, with a length to diameter ratio of about twenty. In some cases, the screw pitch may vary in the streamwise direction, or else the screw may taper along its length to become wider as it approaches the die. The length of the metering section depends on the nature of the material being extruded. Polymeric films and fibers require long metering sections, whereas materials such as UPVC or natural rubber are extruded in shorter sections. The screw may perform twenty or more turns in the metering section with a pitch approximately equal to the screw diame-

Correspondence concerning this article should be addressed to C. Pozrikidis at cpozrikidis@ucsd.edu

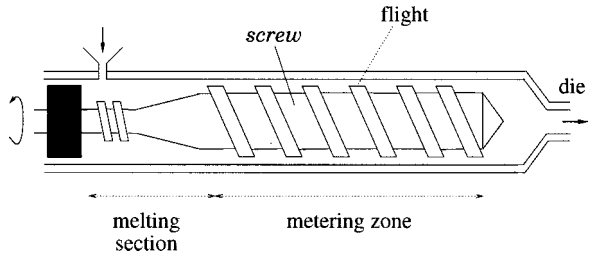

Figure 1. Single-screw extruder showing the melting section and the metering zone.

ter. The rotation rate is typically on the order of one revolution per second. The clearance gap between the flight and the barrel wall is typically small. Loss of efficiency may result from leakage through the flight gap, or from back-pressure resulting from the constriction at the die which inhibits the free ejection of the melt. A positive pressure gradient established along the screw forces material back toward the feeder, opposing the forward motion generated by the rotation.

Seemingly, the first analytical study of flow in a screw extruder was undertaken in 1928 by Rowell and Finlayson[4] working under the auspices of lubrication theory, as reviewed by Carley and Strub.[5] Much later, Booy[6] presented a detailed analysis of the melting zone. In more recent theoretical studies of the metering zone, the helical flow domain is unraveled to furnish the simpler problem of flow in an angled channel. A moving conveyor belt underneath implements the effect of rotation. A classical analysis along these lines was performed by Stevens and Covas[1] who demonstrate that the resulting flow pattern resembles that seen in earlier experiments of a real screw flow by Eccher and Valentinotti.[7] Working in this framework, Kim and Kwon[8,9] developed a "chaos screw" with a view to enhancing mixing via chaotic advection. The key idea is to insert barriers into the unraveled channel flow so as to introduce a hyperbolic node in the cross-sectional streamline pattern. Using both an experimental and a numerical approach, the authors showed barriers significantly enhance the mixing properties. Experiments on the mixing flow occurring in the chaos screw were performed by Hwang, Jun and Kwon.[10] Ghoreishy and Nouri[11] conducted a finite element analysis of the single-extruder flow when the helical domain is unraveled into a channel. Commercially available finite element codes have been used by others to produce results for screw geometries that closely resemble those seen in the production line (for example, O'Brien[12]). Although experimental data on flow through real industrial screws have been collected by several authors (for example, Weert et al.[13]), a fundamental analysis of the flow in a real-life extruder geometry beyond modeling is currently not available.

In this article, we investigate Stokes flow in the helical metering section of a single-screw extruder, with a view to describing the velocity-field around the screw and predicting the flow rate through the barrel. Working with a realistic metering geometry, we make the simplifying, but realistic assumption that the pitch is sufficiently large in comparison to the screw diameter, and perform a perturbation analysis. The use of helical coordinates considerably simplifies the analysis by allowing us to tackle an effectively two-dimensional problem, where all flow variables are independent of the helical streamwise coordinate. At each order of approximation, the resulting problem is solved by finite element methods up to second-order in a properly defined pitch parameter. Despite the simplification of large pitch, recent work by Pozrikidis[14] on flow through twisting pipes suggests that the predictions obtained via this method can be expected to provide a good approximation to the flow for pitches as low as one and half times the screw diameter. Consequently, our calculations should provide valuable insights into a realistic screw flow. In the Problem Formulation section, we define the problem and conduct the perturbation analysis. In the Results section we study a realistic screw geometry and provide values for the flow rate. In the Discussion section, we summarize our findings.

Problem Formulation

We consider helically symmetric Stokes flow through the metering section of a single-screw extruder. The extruder is modeled as a straight circular pipe of radius b filled with a viscous liquid that is stirred by a rotating coaxial helical screw of core radius a, possibly in the presence of an axial pressure gradient. The cross-section of the screw is shown in Figure 2a together with the working system of global Cartesian coordinates. Values for the core radius a, height h, width d, and angle γ of the screw flight will be chosen to correspond to an industrial screw extruder. The helical geometry arises by twisting the screw cross-section at a particular location by an angle that depends linearly on the axial distance x. The pitch, L, is equal to the axial distance required for the cross-section to perform one complete revolution. A typical right-handed screw is shown in Figure 3a, for pitch $L/a = 46.5$, where the counter-clockwise rotation is indicated by the direction of the arrows. In the absence of an opposing pressure gradient, the counterclockwise rotation of a right-handed screw drives a mean axial flow in the positive direction of the x axis.

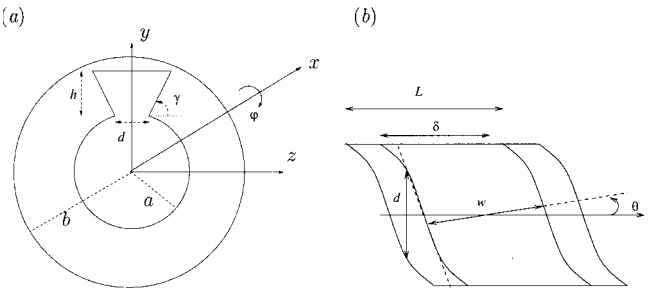

Figure 2. (*a*) Illustration of the screw cross-section with respect to the global Cartesian coordinate system (*x, y, z*), (the azimuthal angle φ, measures rotation around the *x* axis, as shown); (*b*) cross-section of the screw in a plane passing through the *x* axis showing the width of the unraveled channel, *w,* and the helical pitch angle, θ.

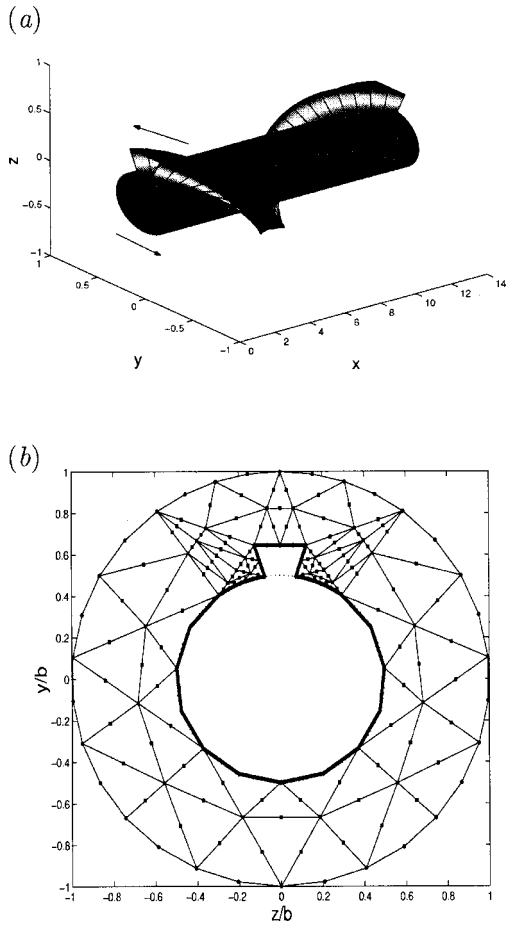

Figure 3. (*a*) A righthanded single-screw with pitch *L*/*a* = 46.5; (*b*) typical first descendant finite-element discretization of the extruder cross-section at *x* = 0.

The contour of the screw itself is shown as a heavy line.

It is convenient to work in the nonorthogonal system of helical coordinates $(\hat{\sigma}, \hat{\varphi}, \hat{x})$ illustrated in Figure 4, defined in relation to the cylindrical polar coordinates (σ, φ, x) as

$$\hat{\sigma} = \sigma, \quad \hat{\varphi} = \varphi - \alpha x, \quad \hat{x} = x \tag{1}$$

where $\alpha \equiv 2\pi/L$ is the wave number defined with respect to the pitch. The helical coordinates are related to the Cartesian coordinates by the relations

$$x = \hat{x}, \quad y = \hat{\sigma}\,\cos(\hat{\varphi} + \alpha\hat{x}), \quad z = \hat{\sigma}\,\sin(\hat{\varphi} + \alpha\hat{x}) \tag{2}$$

In the adopted helical coordinate system, the fluid velocity is expressed as

$$\mathbf{u} = u_{\hat{\sigma}}\mathbf{e}_{\hat{\sigma}} + u_{\hat{\varphi}}\mathbf{e}_{\hat{\varphi}} + u_{\hat{x}}\mathbf{e}_{\hat{x}} \tag{3}$$

where the helical unit vectors are given by $\mathbf{e}_{\hat{\sigma}} = \mathbf{e}_{\sigma}$, $\mathbf{e}_{\hat{\varphi}} = \mathbf{e}_{\varphi}$, and $\mathbf{e}_{\hat{x}} = \frac{1}{H}(\mathbf{e}_x + \alpha\sigma\mathbf{e}_{\varphi})$; $H = (1 + \alpha^2\sigma^2)^{1/2}$, and $\mathbf{e}_{\sigma}$, $\mathbf{e}_{\varphi}$, and $\mathbf{e}_x$ are the unit vectors of the cylindrical polar coordinates. The helical velocity components are related to the cylindrical polar components by

$$u_{\hat{\sigma}} = u_{\sigma}, \quad u_{\hat{\varphi}} = u_{\varphi} - \alpha\sigma u_x, \quad u_{\hat{x}} = Hu_x \tag{4}$$

We assume that the rotating screw produces a helically symmetric flow with no variation of the velocity components in the helical direction indicated by the vector $\mathbf{e}_{\hat{x}}$; for example, $\mathbf{e}_{\hat{x}} \cdot \nabla u_{\hat{\sigma}} \equiv 0$. In addition, we allow for a helically symmetric axial pressure gradient

$$-\left(\frac{\partial p}{\partial \hat{x}}\right)_{\hat{\sigma},\hat{\varphi}} \equiv G \tag{5}$$

Of particular interest is the axial-flow rate,

$$Q = \iint_S u_x\,\hat{\sigma}\,\mathrm{d}\hat{\sigma}\,\mathrm{d}\hat{\varphi} \tag{6}$$

where S is a planar surface normal to the x axis subtended between the screw and the barrel wall.

The equations of steady Stokes flow in helical coordinates were written by Tung and Laurence,[17] and are repeated here for ready reference in slightly altered form. The $\hat{\sigma}$ component reads

$$\frac{1}{\mu}\frac{\partial p}{\partial \hat{\sigma}} = \frac{\partial}{\partial \hat{\sigma}}\left(\frac{1}{\hat{\sigma}}\frac{\partial}{\partial \hat{\sigma}}(\hat{\sigma}\,u_{\hat{\sigma}})\right) + \frac{1}{\hat{\sigma}^2}\frac{\partial^2 u_{\hat{\sigma}}}{\partial \hat{\varphi}^2} - \frac{2}{\hat{\sigma}^2}\frac{\partial u_{\hat{\varphi}}}{\partial \hat{\varphi}} + \alpha F_{\hat{\sigma}} \tag{7}$$

where

$$F_{\hat{\sigma}} \equiv \alpha\frac{\partial^2 u_{\hat{\sigma}}}{\partial \hat{\varphi}^2} - \frac{2}{\hat{\sigma}}\frac{\partial u_x}{\partial \hat{\varphi}} \tag{8}$$

the $\hat{\varphi}$ component reads

$$\frac{1}{\mu}\frac{1}{\hat{\sigma}}\frac{\partial p}{\partial \hat{\varphi}} = \frac{\partial}{\partial \hat{\sigma}}\left(\frac{1}{\hat{\sigma}}\frac{\partial}{\partial \hat{\sigma}}(\hat{\sigma}u_{\hat{\varphi}})\right) + \frac{1}{\hat{\sigma}^2}\frac{\partial^2 u_{\hat{\varphi}}}{\partial \hat{\varphi}^2} + \frac{2}{\hat{\sigma}^2}\frac{\partial u_{\hat{\sigma}}}{\partial \hat{\varphi}} + \alpha F_{\hat{\varphi}} \tag{9}$$

where

$$F_{\hat{\varphi}} = \alpha\frac{\partial^2 u_{\hat{\varphi}}}{\partial \hat{\varphi}^2} + 2\frac{\partial u_x}{\partial \hat{\sigma}} - \frac{1}{\mu}\hat{\sigma}\left(G + \alpha\frac{\partial p}{\partial \hat{\varphi}}\right) \tag{10}$$

and the $\hat{x}$ component reads

$$-\frac{G}{\mu} = \frac{1}{\hat{\sigma}}\frac{\partial}{\partial \hat{\sigma}}\left(\hat{\sigma}\frac{\partial u_x}{\partial \hat{\sigma}}\right) + \frac{1}{\hat{\sigma}^2}\frac{\partial^2 u_x}{\partial \hat{\varphi}^2} + \alpha F\hat{x} \tag{11}$$

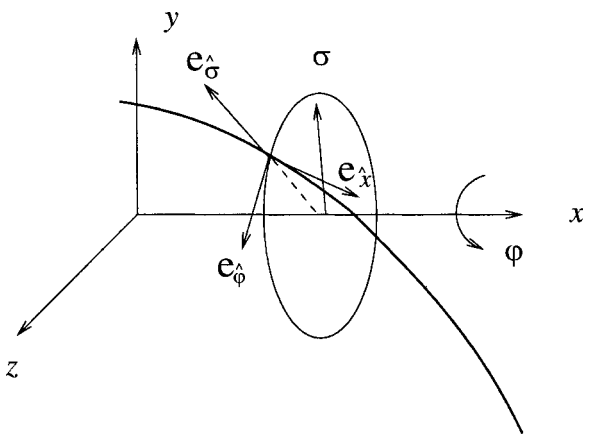

Figure 4. Definition of helical coordinates ($\hat{x}$,$\hat{\sigma}$, $\hat{\varphi}$), in relation to the global Cartesian coordinates and polar cylindrical coordinates (x,σ, φ).

where

$$F_{\hat{x}} \equiv \alpha \frac{\partial^2 u_x}{\partial \hat{\varphi}^2} + \frac{1}{\mu}\frac{\partial p}{\partial \hat{\varphi}} \tag{12}$$

The continuity equation requires

$$\frac{\partial u_{\hat{\sigma}}}{\partial \hat{\sigma}} + \frac{u_{\hat{\sigma}}}{\hat{\sigma}} + \frac{1}{\hat{\sigma}}\frac{\partial u_{\hat{\varphi}}}{\partial \hat{\varphi}} = 0 \tag{13}$$

We proceed by assuming that the pitch is long compared to the barrel radius, and perform a perturbation analysis to determine the solution at successive orders of approximation for a small dimensionless parameter $\beta \equiv \alpha b = 2\pi b/L$.

Pressure-driven flow

In the case of pressure-driven flow with a stationary screw, $\Omega = 0$, $G \neq 0$, we follow a recent analysis for flow through a twisted tube,[14] and write the asymptotic expansion

$$u_{\hat{\sigma}} = \beta\, u_{\hat{\sigma}}^{(1)} + \beta^2\, u_{\hat{\sigma}}^{(2)} + \cdots, \quad u_{\hat{\varphi}} = \beta\, u_{\hat{\varphi}}^{(1)} + \beta^2\, u_{\hat{\varphi}}^{(2)} + \cdots$$
$$u_x = u_x^{(0)} + \beta\, u_x^{(1)} + \beta^2 u_x^{(2)} + \cdots,$$
$$p = p^{(0)} + \beta p^{(1)} + \beta^2 p^{(2)} + \cdots \tag{14}$$

Using the second equation in (4), we find that the physical azimuthal velocity component is given by the perturbation expansion

$$u_\varphi = u_{\hat{\varphi}} + \beta\,\frac{\hat{\sigma}}{a}\,u_x = \beta\left(u_{\hat{\varphi}}^{(1)} + \frac{\hat{\sigma}}{a}\,u_x^{(0)}\right) + \beta^2\left(u_{\hat{\varphi}}^{(2)} + \frac{\hat{\sigma}}{a}\,u_x^{(1)}\right) + \cdots \tag{15}$$

All velocities are required to be zero around the tube contour.

The zero-order axial-velocity field satisfies the equations of unidirectional tube flow with a linear-pressure field, $p^{(0)} = -G\hat{x}$,

$$\hat{\nabla}^2 u_x^{(0)} = -\frac{G}{\mu} \tag{16}$$

where $\hat{\nabla}^2 = \partial^2/\partial\hat{y}^2 + \partial^2/\partial\hat{z}^2$ is the Laplacian in the $\hat{y}\,\hat{z}$ plane, defined such that $\hat{y} = \hat{\sigma}\cos\hat{\varphi}$ and $\hat{z} = \hat{\sigma}\sin\hat{\varphi}$.

The first-order field satisfies the equations

$$\frac{1}{\mu}\frac{\partial p^{(1)}}{\partial \hat{\sigma}} = \frac{\partial}{\partial \hat{\sigma}}\left(\frac{1}{\hat{\sigma}}\frac{\partial}{\partial \hat{\sigma}}\left(\hat{\sigma}\, u_{\hat{\sigma}}^{(1)}\right)\right) + \frac{1}{\hat{\sigma}^2}\frac{\partial^2 u_{\hat{\sigma}}^{(1)}}{\partial \hat{\varphi}^2} - \frac{2}{\hat{\sigma}^2}\frac{\partial u_{\hat{\varphi}}^{(1)}}{\partial \hat{\varphi}} - \frac{2}{a\,\hat{\sigma}}\frac{\partial u_x^{(0)}}{\partial \hat{\varphi}} \tag{17}$$

$$\frac{1}{\mu}\frac{1}{\hat{\sigma}}\frac{\partial p^{(1)}}{\partial \hat{\varphi}} = \frac{\partial}{\partial \hat{\sigma}}\left(\frac{1}{\hat{\sigma}}\frac{\partial}{\partial \hat{\sigma}}\left(\hat{\sigma}\, u_{\hat{\varphi}}^{(1)}\right)\right) + \frac{1}{\hat{\sigma}^2}\frac{\partial^2 u_{\hat{\varphi}}^{(1)}}{\partial \hat{\varphi}^2} + \frac{2}{\hat{\sigma}^2}\frac{\partial u_{\hat{\sigma}}^{(1)}}{\partial \hat{\varphi}} + \frac{2}{a}\frac{\partial u_x^{(0)}}{\partial \hat{\sigma}} - \frac{\hat{\sigma}G}{\mu a} \tag{18}$$

$$\hat{\nabla}^2 u_x^{(1)} = 0 \tag{19}$$

complemented by the continuity equation

$$\frac{1}{\hat{\sigma}}\left(\frac{\partial(\hat{\sigma}u_{\hat{\sigma}}^{(1)})}{\partial \hat{\sigma}} + \frac{\partial u_{\hat{\varphi}}^{(1)}}{\partial \hat{\varphi}}\right) = 0 \tag{20}$$

The solution of (Eq. 19) is $u_x^{(1)} = 0$, which shows that the first-order velocity contributes neither to the axial flow nor to the axial flow rate. In Cartesian coordinates ($\hat{y}$, $\hat{z}$), Eqs. 17 and 18 describing flow in a plane that is perpendicular to the x axis combine into the forced Stokes equation

where $$\hat{\nabla} p^{(1)} = \mu \hat{\nabla}^2 \hat{u}^{(1)} + \mathbf{b} \tag{21}$$

$$\mathbf{b} = \mu\, \mathbf{e}_x \times \frac{2}{a}\hat{\nabla} u_x^{(0)} - \frac{\hat{\sigma}G}{a}\,\mathbf{e}_{\hat{\varphi}} \tag{22}$$

is the body force, $\mathbf{e}_x$ is the unit vector along the x axis, $\mathbf{e}_{\hat{\varphi}} = (-\hat{z}/\hat{\sigma}, \hat{y}/\hat{\sigma})$ is the unit vector along the $\hat{\varphi}$ axis, $\hat{\mathbf{u}}^{(1)} = (\hat{u}_{\hat{y}}^{(1)}, \hat{u}_{\hat{z}}^{(1)})$, and $\hat{\nabla} = (\partial/\partial\hat{y}, \partial/\partial\hat{z})$ is the gradient in the $\hat{y}\,\hat{z}$ plane.

Explicitly

$$\mathrm{b} = \frac{2\mu}{a}\begin{bmatrix} -\partial u_x^{(0)}/\partial\hat{z} \\ \partial u_x^{(0)}/\partial\hat{y} \end{bmatrix} - \frac{G}{a}\begin{bmatrix} -\hat{z} \\ \hat{y} \end{bmatrix} \tag{23}$$

The continuity equation requires

$$\hat{\nabla}\cdot\hat{\mathbf{u}}^{(1)} = 0 \tag{24}$$

Equations 21 and 24 describe a forced Stokes flow problem over the tube cross-section, where the body-force term depends on the velocity gradient of the zeroth-order unidirectional flow.

The second-order axial velocity satisfies the Poisson equation

$$\hat{\nabla}^2 u_x^{(2)} + \frac{1}{a^2}\frac{\partial^2 u_x^{(0)}}{\partial \hat{\varphi}^2} + \frac{1}{\mu a}\frac{\partial p^{(1)}}{\partial \hat{\varphi}} = 0 \tag{25}$$

which can be restated in the computationally preferred form

$$\hat{\nabla}^2 u_x^{(2)} - \frac{G}{\mu}\frac{\hat{\sigma}^2}{a^2} - \frac{\hat{\sigma}}{a^2}\frac{\partial}{\partial\hat{\sigma}}\left(\hat{\sigma}\frac{\partial u_x^{(0)}}{\partial\hat{\sigma}}\right) + \frac{1}{\mu a}\mathbf{e}_{\hat{\varphi}}\cdot\nabla p^{(1)} = 0 \tag{26}$$

In the absence of rotation, there is a contribution to the flow rate at leading and second order but not at first order, yielding the asymptotic expansion

$$Q_P = \frac{G\pi b^4}{8\mu}\left[q_P^{(0)} + \beta^2\, q_P^{(2)} + \cdots\right] \tag{27}$$

In the next section, we shall tabulate the computed dimensionless flow rate coefficients $q_P^{(0)}$ and $q_P^{(2)}$.

The zeroth- and second-order problems were solved using a finite element method for unidirectional flow governed by the Poisson equation, and the second-order problem was solved using a finite element method for 2-D Stokes flow.[15] To implement the method for the screw geometry, we manually discretize the cross-section into a network of seventeen six-node triangular elements, each with a node at every vertex and a midnode lying midway along each edge. Refinement of this parental grid is achieved by successive subdivision of the network into a nested sequence of subtriangles;

an example corresponding to one subdivisional step from the parental structure is shown in Figure 3b. The slight distortion of the individual triangular elements is due to the projection of the mid-nodes along the element edges representing the circular body of the screw onto $\hat{\sigma} = a$. In the case of the Poisson equation governing the zeroth- and second-order flow, the unknown streamwise velocity is approximated with a quadratic function over each element. In the case of Stokes flow, each velocity component is approximated with a quadratic function and the pressure is approximated with a constant function over each element.

Rotation-driven flow

To study the flow generated by the rotation of the screw, we set $G = 0$ and expand the flow variables as

$$u_{\hat{\sigma}} = u_{\hat{\sigma}}^{(0)} + \beta u_{\hat{\sigma}}^{(1)} + \beta^2 u_{\hat{\sigma}}^{(2)} + \cdots, u_{\hat{\varphi}} = u_{\hat{\varphi}}^{(0)} + \beta u_{\hat{\varphi}}^{(1)} + \beta^2 u_{\hat{\varphi}}^{(2)} + \cdots$$
$$u_x = \beta\, u_x^{(1)} + \beta^2\, u_x^{(2)} + \cdots, \quad p = p^{(0)} + \beta\, p^{(1)} + \beta^2 p^{(2)} + \cdots \tag{28}$$

Under the assumption of helical symmetry, all functions in these expansions are independent of $\hat{x}$. According to Eq. 4, the physical azimuthal velocity component is expanded as

$$u_{\varphi} = u_{\hat{\varphi}}^{(0)} + \beta\, u_{\hat{\varphi}}^{(1)} + \beta^2 \left(u_{\hat{\varphi}}^{(2)} + \frac{\hat{\sigma} u_x^{(1)}}{b} \right) + \cdots. \tag{29}$$

Substituting these expansions in the governing Eqs. 7–13, we obtain at leading order

$$-\nabla p^{(0)} + \mu \nabla^2 \mathbf{u}^{(0)} = \mathbf{0}, \qquad \nabla \cdot \mathbf{u}^{(0)} = 0 \tag{30}$$

governing two-dimensional Stokes flow over the cross-section, where $\mathbf{u}^{(0)} = u_{\hat{\sigma}}^{(0)} \mathbf{e}_{\hat{\sigma}} + u_{\hat{\varphi}}^{(0)} \mathbf{e}_{\hat{\varphi}}$. The boundary conditions require $u_{\hat{\sigma}}^{(0)} = 0$ and $u_{\hat{\varphi}}^{(0)} = \hat{\sigma}\Omega$ on the screw, and $u_{\hat{\sigma}}^{(0)} = u_{\hat{\sigma}}^{(0)} = 0$ at the barrel wall $\hat{\sigma} = b$, where Ω is the angular velocity of rotation. At first-order $O(\beta)$, we find $u_{\hat{\sigma}}^{(1)} = u_{\hat{\varphi}}^{(1)} = 0$ everywhere in the flow domain. The axial velocity satisfies the Poisson equation

$$\nabla^2 u_x^{(1)} + \frac{1}{b\mu} \frac{\partial p^{(0)}}{\partial \hat{\varphi}} = 0 \tag{31}$$

subject to the boundary condition $u_x^{(1)} = 0$ both on the screw and the barrel wall. The source term represented by the second term on the left-hand side is known in numerical form from the solution of the leading-order problem. At second-order $O(\beta^2)$, we derive the forced Stokes flow problem

$$-\nabla p^{(2)} + \mu \nabla^2 \mathbf{u}^{(2)} + \mathbf{b} = \mathbf{0}, \qquad \nabla \cdot \mathbf{u}^{(2)} = 0 \tag{32}$$

where $\mathbf{u}^{(2)} = u_{\hat{\sigma}}^{(2)} \mathbf{e}_{\hat{\sigma}} + u_{\hat{\varphi}}^{(2)} \mathbf{e}_{\hat{\varphi}}$, and the body force is given by

$$\mathbf{b} = \frac{\mu}{b} \left[\left(\frac{1}{b} \frac{\partial^2 u_{\hat{\sigma}}^{(0)}}{\partial \hat{\varphi}^2} - \frac{2}{\hat{\sigma}} \frac{\partial u_x^{(1)}}{\partial \hat{\varphi}} \right) \mathbf{e}_{\hat{\sigma}} + \left(\frac{1}{b} \frac{\partial^2 u_{\hat{\varphi}}^{(0)}}{\partial \hat{\varphi}^2} + 2 \frac{\partial u_x^{(1)}}{\partial \hat{\sigma}} - \frac{\hat{\sigma}}{\mu b} \frac{\partial p^{(0)}}{\partial \hat{\varphi}} \right) \mathbf{e}_{\hat{\varphi}} \right] \tag{33}$$

which can be restated as

$$\mathbf{b} = \frac{\mu}{b^2} \mathcal{L}^2 u_{\hat{\sigma}}^{(0)} \mathbf{e}_{\hat{\sigma}} + \frac{\mu}{b^2} \mathcal{L}^2 u_{\hat{\varphi}}^{(0)} \mathbf{e}_{\hat{\varphi}} + \mu \mathbf{e}_x \times \frac{2}{b} \hat{\nabla} u_x^{(1)} - \frac{\hat{\sigma}}{b^2} \mathcal{L} p^{(0)} \mathbf{e}_{\hat{\varphi}} \tag{34}$$

where $\mathcal{L} u_{\hat{\sigma}}^{(0)} \equiv (-\hat{z}, \hat{y}) \cdot \hat{\nabla} u_{\hat{\sigma}}^{(0)}$. The boundary conditions require $u_{\hat{\sigma}}^{(2)} = u_{\hat{\varphi}}^{(2)} = 0$ both on the screw and barrel wall. Because the axial component $u_x^{(2)}$ is identically zero, there is no contribution to the flow rate at this order. The expansion for the flow rate may, therefore, be written as

$$Q_R = \Omega b^3 \beta \left[q_R + O(\beta^2) \right] \tag{35}$$

where the dimensionless coefficient q_R may be computed from the solution of the first-order problem governed by Eq. 31. The first three problems were solved using the finite-element methods discussed previously for pressure-driven flow.

Results

We shall present results for the two modular cases of pressure-driven and rotation-driven flow, bearing in mind that linearity allows us to superimpose the solutions.

Pressure-driven flow

In the case of pressure-driven flow with a stationary screw, $G \neq 0$ and $\Omega = 0$. Figure 5 shows the profiles of the computed zeroth-order unidirectional flow, and second-order axial flow for $a/b = 0.5$, $w/a = 1/3$, $\gamma = \pi/2$, and $h/b = 0.4$. The second-order flow is directed toward the negative direction of the x axis over the entire cross-section, except near the gap where forward-flow occurs. Nevertheless, it is clear that

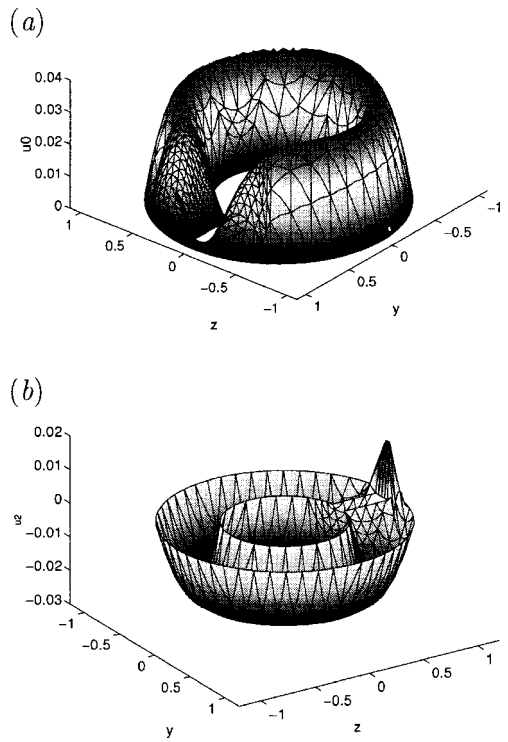

Figure 5. Pressure-driven flow: axial velocity profiles of the (*a*) zeroth-order, and (*b*) second-order flow for an extruder with $a/b = 0.5$, $w/a = 1/3$, $\gamma = \pi/2$, and $h/b = 0.4$.

The velocity displayed has been reduced by Gb^2/μ.

Table 1. Flow rate Coefficients $q_P^{(0)}$ and $q_P^{(2)}$ for Pressure-Driven flow in an Extruder with (a) $\gamma = \pi/2$, $d = a/3$, $a/b = 0.5$ and Various Screw-head Heights, h/b. (b) $\gamma = \pi/2$, $d/a = 1/3$, $h/a = 1/5$, and Various Radii Ratios a/b.

(a)				(b)			
h/b	ε	$q_P^{(0)}$	$q_P^{(2)}$	a/b	ε	$q_P^{(0)}$	$q_P^{(2)}$
0.0	0.5	0.126	0.0	0.0	1.0	1.0	0.0
0.1	0.4	0.121	−0.003	0.4	0.52	0.198	−0.001
0.2	0.3	0.116	−0.016	0.5	0.40	0.121	−0.003
0.3	0.2	0.114	−0.041	0.6	0.28	0.065	−0.004
0.4	0.1	0.113	−0.07	0.7	0.16	0.029	−0.005

The dimensionless gap between the wall and the flight, $\varepsilon = 1 - (h + a)/b$, is shown in the second column.

the second-order flow rate will be negative, reflecting an overwhelming perturbation back-flow.

Table 1*a* lists the flow rate coefficients for $\gamma = \pi/2$, $d/a = 1/3$, $a/b = 1/2$, and varying flight size h, computed with 320 elements. The discretization level was increased until results were obtained accurate to two or three decimal places, as shown. The computations show that the leading-order flow rate $q^{(0)}$, decreases as the gap between the flight and the wall is reduced. In the case of pressure-driven flow through an annular tube, the well-known analytical solution predicts[16]

$$q^{(0)} = (1 - \delta^2)\left(1 + \delta^2 + \frac{1 - \delta^2}{\log \delta}\right) \tag{36}$$

where $\delta = a/b$. The computed values for a non-zero h are close to the prediction of this formula, shown in the first line of Table 1*a*, even though the limit $h \to 0$ yields a circular screw with a flattened top. Because the helical twist of the screw lowers the flow rate for a fixed pressure gradient, the coefficient $q_P^{(2)}$ is negative in all cases, resulting in additional energy requirements. Choosing $\gamma = \pi/2$, $d/a = 1/3$, and $h/a = 1/5$ with reference to Figure 2, yields shapes similar to those encountered in industrial settings. Results for the flow rate coefficients are presented in Table 1*b* for several values of the radii ratio a/b. The calculations were performed with 608 elements for $a/b = 0.4$, 320 elements for $a/b = 0.5$ and 0.6, and with 416 elements for $a/b = 0.7$. The second-order flow rate is negative in all cases, revealing back-flow.

When the gap between the flight and the outer cylinder is small, $\varepsilon \simeq 0$, as the pitch is reduced, the flow along the quadrilateral grooves resembles pressure-driven flow through a two-dimensional channel with height $H = b - a$ confined from above and below by two parallel walls, and from left and right by two-side walls slanted at the angle γ. When $\gamma = \pi/2$, the side walls are parallel yielding a rectangular geometry. With reference to Figure 2b, the channel width is $w = \delta \cos\theta$, where $\delta \simeq L - d \tan\theta$. Unraveling the channel, we find that the pitch angle θ is given by $\tan\theta = L/(2\pi b)$; thus $w \simeq L \cos\theta - d \sin\theta$. Using the well-known Boussinesq series solution,[16] we find the predicted flow rate for pressure-driven channel flow

$$Q_{PC} = \frac{G_C w H^3}{12\mu} F\left(\frac{w}{H}\right), \qquad F(x) = 1 - \frac{6}{x}\sum_{n=1}^{\infty} \frac{\tanh(\alpha_n x)}{\alpha_n^5} \tag{37}$$

where $\alpha_n = (2n - 1)\pi/2$ and $G_C = G\cos\theta$ is the pressure gradient along the groove (see, for example, Pozrikidis[16]). Figure 6a illustrates the ratio between the flow rate predicted by the present analysis, and that predicted by the channel flow model as a function of the pitch L/b for the smallest gap considered corresponding to width $h/b = 0.4$. For large values of the pitch, the asymptotic result is accurate, but the actual flow is poorly represented by the channel flow (Eq. 37). The opposite holds true for small pitch, and the best agreement should be obtained somewhere between the two extremes, as is found in the graph. In fact, the channel flow (Eq. 37) yields a best approximation for the flow rate when $L/b \approx 11$.

Rotation-driven flow

Next, we turn our attention to flow generated by the screw rotation in the absence of an applied axial-pressure gradient, $G = 0$ and $\Omega \neq 0$. As in the case of pressure-driven flow, we focus our attention on realistic parameter values. In Figure 7a, the flow rate coefficient q_R is plotted against flight-size for $a/b = 0.5$, $\gamma = \pi/2$, and $d = a/3$. Since q_R is positive, the computations confirm that the counterclockwise rotation drives a mean flow in the positive direction of the x axis. As the reduced height h/b approaches zero, the screw geometry resembles a rotating cylinder independent of the pitch, and the downstream flow rate tends to vanish. On the contrary, as the gap between the wall and the screw head narrows down, the flow rate increases rapidly. Similar results are obtained when the flight size is fixed and the screw radius is increased, as shown in Figure 7b. The calculations become inaccurate for very small gaps outside the range shown in the figures. When $h/b = 0$, a discontinuity in the

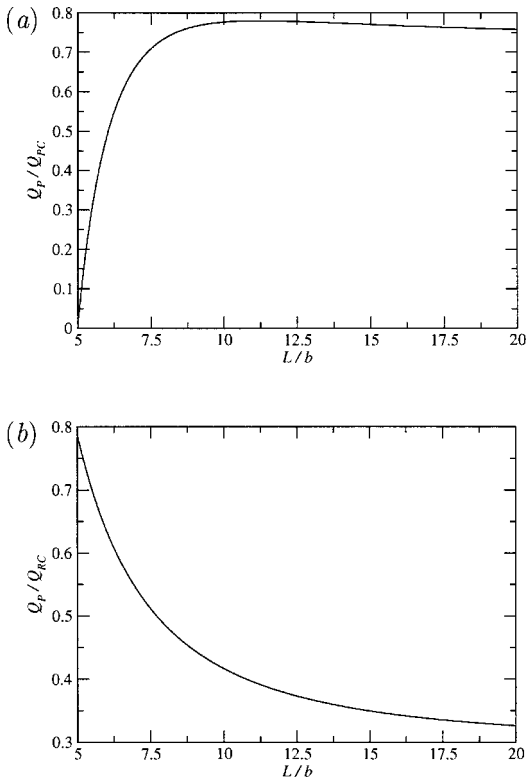

Figure 6. Flow rate ratio (*a*) Q_P/Q_{PC}, and (*b*) Q_R/Q_{RC} plotted against the dimensionless pitch L/b for $\gamma = \pi/2$, $d = a/3$, $a/b = 0.5$, and $h/b = 0.4$.

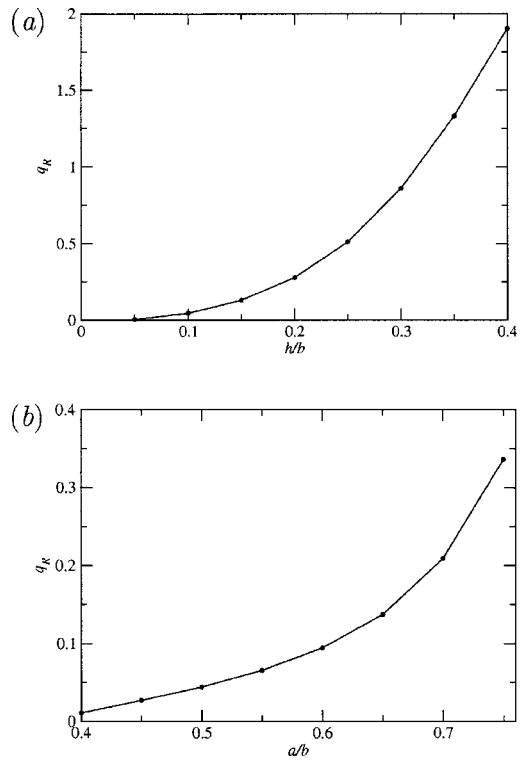

Figure 7. Flow rate q_R, for $\gamma = \pi/2$, $d = a/3$, and (a) $a/b = 0.5$ with varying screw-head height h/b, or (b) $h = a/5$ with varying a/b.

velocity occurs at the sharp corner, yielding an unphysical non-integrable stress that requires an infinite torque to sustain the rotation. In a real-life screw extruder, the gap between the flight and the wall tends to be very small, typically less than 0.15% of the diameter (Stevens and Covas[1]). The results shown in Figure 7 suggest that the flow rate will continue to increase sharply as the gap is closed.

Figure 8 illustrates the physical zeroth-order velocity field in an axial plane, and the first-order axial velocity profile for a screw with $\gamma = \pi/2$, $a/b = 0.5$, $d/a = 1/3$ and $h/a = 0.2$ and 0.4. The first-order axial velocity is positive over the entire annular cross-section, except inside the small gap where back flow occurs. On balance, the forward flow dominates the backward flow and yields a positive flow rate. Figure 9 shows a close-up of the velocity field for a screw with $a/b = 0.8$, $\gamma = \pi/2$, $h/b = 0.15$, and $d = 0.2$, corresponding to a barrel-flight clearance of $0.05b$, computed with 416 elements. The field arrows are proportional in length to the magnitude of the local-velocity vector. The flow is observed in a frame of reference moving with the rotating screw so that the barrel wall appears to be moving clockwise. In the remainder of the domain, the flow field resembles rigid body motion. At first-order, the velocity intensifies in magnitude slightly as the fluid negotiates the gap above the flight. However, the second-order contribution opposes this motion and slightly reduces the gap velocity.

When the gap between the flight and the outer cylinder is small, $\varepsilon \simeq 0$, as the pitch is reduced, the flow along the quadrilateral grooves resembles unidirectional flow through a two-dimensional channel with clearance $c = b - a$, and width $w = L \cos\theta - d \sin\theta$, driven by the translation of the upper wall, as discussed previously for pressure-driven flow. Rowell and Finlayson[4,5] computed the flow rate as

$$Q_{RC} = \pi\Omega\,(2a + h)\cos\theta\, w^2\, F\left(\frac{2c}{w}\right),$$

$$F(x) = \sum_{n=1}^{\infty} \frac{\cosh(\alpha_n x) - 1}{\alpha_n^3 \sinh(\alpha_n x)}. \qquad (38)$$

Figure 6b illustrates the ratio between the flow rate predicted by the present analysis and that predicted by the channel flow model as a function of the pitch L/b, for the smallest gap considered corresponding to width $h/b = 0.4$. The asymptotic result is accurate for large pitch, while the channel flow result (Eq. 38) is accurate for small pitch, so that good agreement between the two is expected somewhere between the two extremes. This is confirmed by the graph, which shows that the channel flow rate gives a best approximation at $L/b \approx 6$.

Next, we investigate the flow kinematics by studying the advection of point particles in this helical flow. Figure 10 depicts the various locations of four-point particles at different times for one particular screw configuration. All panels show the relative positions of the particles in a plane normal to the x axis. At time $\Omega t = 0$, the orientation of the screw is as shown, and the particles lie at the four vertices of a small square, as indicated in figure 10a. The separate panels show snapshots at

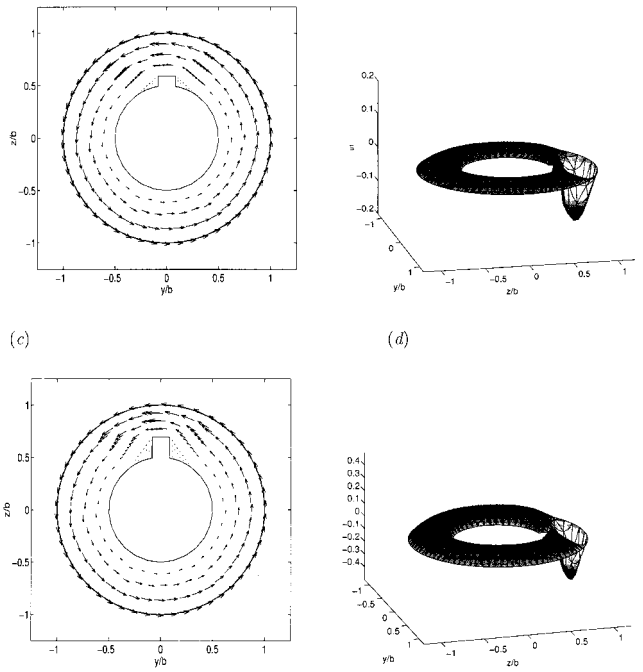

Figure 8. Rotation-driven flow for a screw with $\gamma = \pi/2$, $a/b = 0.5$, $d/a = 1/3$, computed with 608 finite elements: (a, b) Leading-order physical velocity vector field in an axial plane, and first-order axial velocity $u_x^{(1)}$, for $h/a = 0.2$; (c, d) their counterparts for $h/a = 0.4$.

The leading-order flows are visualized in a frame of reference where the wall rotates around the screw.

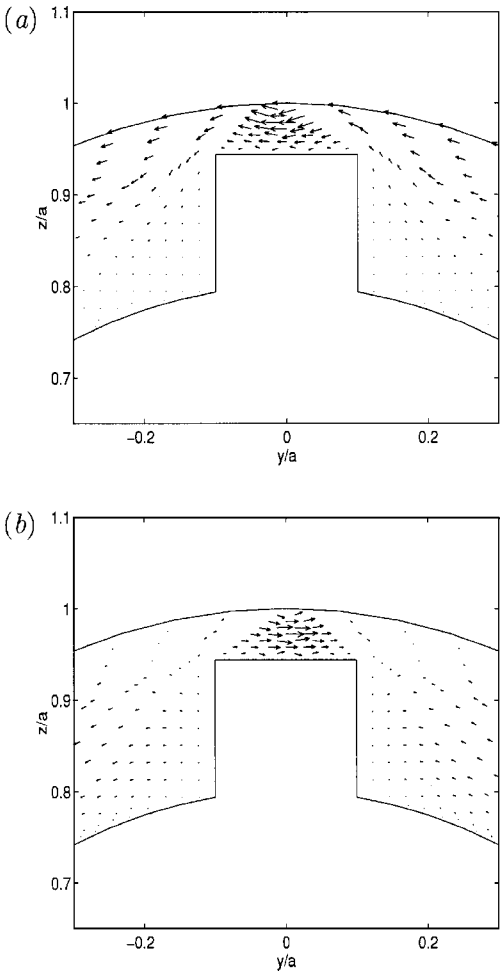

Figure 9. Physical velocity fields in an axial plane shown near the flight of a screw extruder with a/b = 0.8, $\gamma = \pi/2$, h/b = 0.15, and d/b = 0.2.

(*a*) Leading-order field shown with the wall rotating around the screw, and (*b*) second-order velocity field.

various times up to $\Omega t = 19.95$ corresponding to Figure 10f; by this time, the screw has undergone just over three full rotations. The illustrations reveal that the relative positions of the particles change markedly over the course of the flow. Note that the diamond-shaped particle is caught by the screw-head just after the time shown in Figure 10b and dragged for some distance before being released, so accelerating it rapidly away from the remaining particles. A movie generated using Matlab showing the transit of the particles is available from the website www.mth.uea.ac.uk/∼h007.

It should be noted that at any given time, the particles shown in figure 10(*a–f*) are located at different downstream positions. This is demonstrated in figure 10g, where the downstream location of each particle is shown at times corresponding to Figure 10a–f. Near the beginning of the simulation, the particles marked with a circle and a triangle travel a short distance upstream before being carried downstream, and this is repeated after regular intervals. The reason is apparent from the first-order velocity field plotted in Figure 8, where it is shown that the axial component $u_x^{(1)}$, is positive over most of the flow-field except inside the gap between the flight and the barrel wall where it is negative. When a particle enters the gap, it experiences a short period of upstream motion before it is carried out of the gap and into the region of positive axial flow.

Figure 11 shows 3-D particle paths in the fixed (x, y, z) frame for three different values of the pitch parameter β. The geometry of the screw is identical to that shown in Figure 10. The particles are convected with the flow from $\Omega t = 0$ to 9.95, which covers approximately 1.6 full rotations. The small circles show the starting positions, and the crosses show the end positions of particles on each of the three curves. All particles start out at the point $x = 0$, $y = 0.70$, $z = 0.06$ at $\Omega t = 0$. The solid line shows the path for $\beta = 0.05$, corresponding to the circular particle in Figure 10. The lightly-dotted and heavily-dotted lines represent trajectories, respectively, for $\beta = 0.25$ and 0.45. The configuration for $\beta = 0.45$ corresponds to the screw shown in Figure 3a.

Pozrikidis[14] conducted a large-pitch perturbation analysis for pressure-driven flow in a twisted tube, and found that the second-order results are accurate roughly for wave lengths $L > \pi$ or $\beta < 2$. This suggests that the present results should be well within the limitations of the asymptotic theory. Evi-

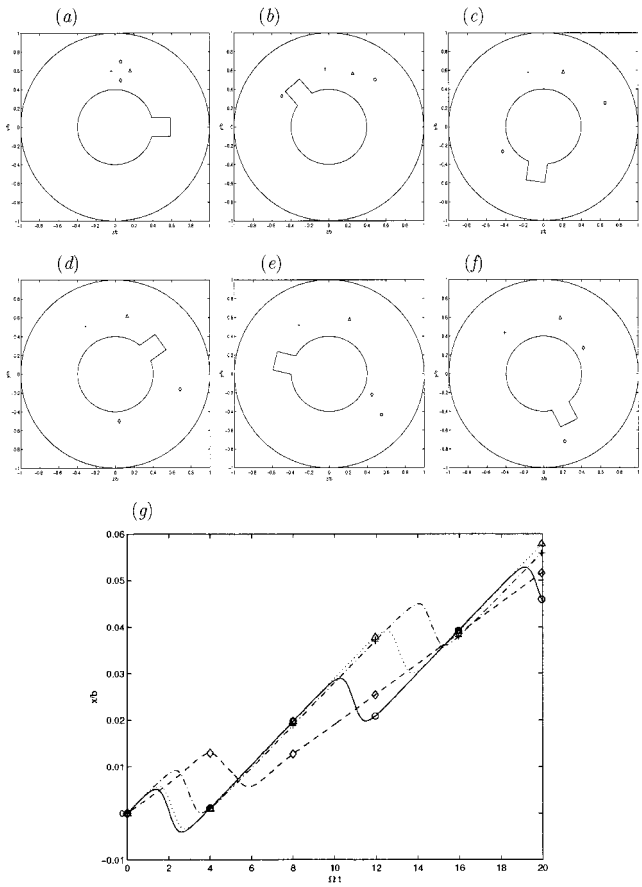

Figure 10. Point particles convected with the flow in a plane normal to the x axis, with the screw rotating in the counter-clockwise direction.

The relative positions of the particles are shown at times (*a*) $\Omega t = 0$, (*b*) 4.0, (*c*) 8.0, (*d*) 11.95, (*e*) 15.95, and (*f*) 19.95. Corresponding downstream positions are shown in (*g*). The symbols correspond to the respective times shown in that figure.

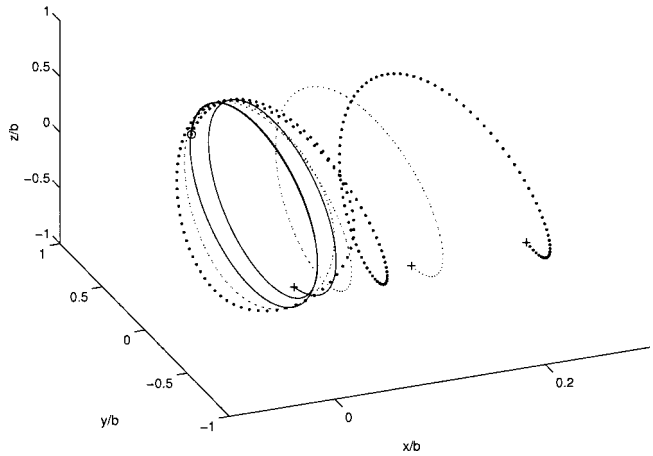

Figure 11. Particle paths in the fixed (*x, y, z*) frame for $\beta = 0.05$ (solid line), 0.25 (light dots), and 0.45 (heavy dots) from $\Omega t = 0$ up to 9.95.

The screw is rotating counter-clockwise about the x axis.

dently, the larger the value of β, and the smaller the pitch, the further particles are carried downstream over equal time intervals. As noted earlier, particles travel a short distance upstream before being convected downstream. The amount of upstream carry decreases as the pitch gets larger.

Discussion

We have conducted a computational study of fluid flow in a single-screw extruder. Working under the auspices of the Stokes approximation, we have performed a perturbation analysis on the assumption of large pitch compared to the screw diameter. In the case of purely pressure-driven flow, there is a contribution to the flow rate at both first and second order. Following the analysis of Pozrikidis,[14] we computed both contributions by solving the individual problems using finite element methods. The second-order contribution is negative indicating that the effect of the screw pitch is to lower the flow rate through the barrel. As the gap between the barrel wall and the screw flight is closed, either by increasing the core radius of the screw or by increasing the size of the flight, the effect of the pitch becomes more pronounced and the second-order flow rate deficit is raised.

In the case of pure rotation, the leading-order problem corresponds to two-dimensional Stokes flow in an axial plane. The first contribution to the axial flow rate arises at first-order and satisfies a Poisson equation with a source term dependent on the leading-order pressure field. The second-order problem equates to Stokes flow in an axial plane with a source term dependent on the leading-order pressure field. If the flight is removed, the problem reduces to that of annular flow between rotating cylinders with circular streamlines. Introducing the helical flight has a marked influence on the trajectory of particles placed within the flow. Particles starting in the same axial plane travel different distances downstream depending on their initial location within the plane. They may become caught by the revolving flight and carried far afield from their counterparts in a short time period. On average, particles drift downstream, but they are also convected upstream in short bursts due to the negative part of the first-order axial velocity profile. Increasing the pitch raises the downstream distance traveled by particles in a given amount of time. As for pressure-driven flow, the axial flow rate depends strongly on the gap between the flight and the barrel wall. As the gap is reduced, either by increasing the size of the flight or by increasing the core radius of the screw, the axial flow rate increases.

In practice, a real screw extruder experiences both pure rotation and a positive pressure gradient, tending to force fluid back up the barrel towards the inlet. The combined effects of rotation-driven and pressure-driven flow may be obtained from the current results through linear superposition.

Acknowledgments

This research was supported by a grant provided by the National Science Foundation. MGB was supported by the Nuffield Foundation under grant NUF-NAL-O4.

Literature Cited

1. Stevens MJ, Covas JA. *Extruder Principles and Operation*. London: Chapman and Hall; 1995.
2. Adams MJ, Briscoe, BJ. The optimisation of solid food processing operations. *Trans Inst Chem Eng*. 1993;C71:251–263.
3. Lee, ST, Ramesh, NS. *Polymeric Foams*. Boca Raton: CRC Press; 2004.
4. Rowell HS, Finlayson D. Screw viscosity pumps. *Engineering* 1928;126:249.
5. Carley JF, Strub, RA. Basic concepts of extrusion. *Ind Eng Chem*. 1953;45:970–973.
6. Booy, ML. Influence of channel curvature on flow, pressure distribution, and power requirement of screw pumps and melt extruders. *SPE Trans*. 1963;3:176.
7. Eccher S, Valentinotti A. Experimental determination of velocity profiles in an extruder screw. *Ind Eng Chem*. 1958;50:829–836.
8. Kim SJ, Kwon TH. Enhancement of mixing performance of single-screw extrusion processes via chaotic flow: Part I. Basic concepts and experimental study. *Adv Polym Tech*. 1996;15:41–54.
9. Kim SJ, Kwon TH. Enhancement of mixing performance of single-screw extrusion processes via chaotic flow: Part II. Numerical study. *Adv Polym Tech*. 1996;15:55–69.
10. Hwang WR, Jun HS, Kwon TH. Experiments on chaotic mixing in a screw channel flow. *AIChE J*. 2002;48:1621–1630.
11. Ghoreishy MHR, Nouri MR. Finite element analysis of thermoplastic melts flow through the metering and die regions of single-screw extruders. *J Appl Poly Sci*. 1999;74:676.
12. O'Brien KT. *Computer Modeling for Extrusion and other Continuous Polymer Processes*. Munich: Hanser; 1992.
13. Weert X, Lawrence CJ, Adams MJ, Briscoe BJ. Screw extrusion of food powders: prediction and performance. *Chem Eng Sci*. 2001;56: 1933–1949.
14. Pozrikidis C. Stokes flow through a twisted tube. *J Fluid Mech*. 2006;567:261–280.
15. Pozrikidis C. *Introduction to Finite and Spectral Element Methods using Matlab*. Boca Raton: Chapman, Hall/CRC; 2005.
16. Pozrikidis C. *Introduction to Theoretical and Computational Fluid Dynamics*. Oxford: Oxford University Press; 1997.
17. Tung TT, Laurence RL. A coordinate frame for helical flows. *Polym Eng Sci*. 1975;15:401–405.

Manuscript received May 17, 2006, and revision received Sept. 28, 2006.